photonics

MDPI

Article

Noise Measurements and Noise Statistical Properties Investigations in a Stimulated Raman Scattering Microscope Based on Three Femtoseconds Laser Sources

Rajeev Ranjan [1,2], Giovanni Costa [1,3], Maria Antonietta Ferrara [1], Mario Sansone [3] and Luigi Sirleto [1,*]

[1] National Research Council (CNR), Institute of Applied Sciences and Intelligent Systems, 80131 Napoli, Italy
[2] CNRS, Centrale Marseille, Institut Fresnel, Aix Marseille Univ, F-13013 Marseille, France
[3] Department of Electrical Engineering and Information Technologies (DIETI), University "Federico II" of Naples, 80125 Naples, Italy
* Correspondence: luigi.sirleto@cnr.it

Abstract: To induce a Raman-active transition in a material, stimulated Raman scattering (SRS) spectroscopy/microscopy implementations typically rely on two pulsed laser sources. One of their limitations is that not all of the regions of Raman spectra can be investigated, so only some applications can be exploited. In this paper, the noise characterizations of a stimulated Raman scattering spectroscopy/microscopy implementation, based on the insertion of a third pulsed laser source, are provided. The merit of this system is that it is able to explore the large variety of SRS applications. In order to characterize our system, an investigation of different kinds of noises due to the laser sources and electronics sources was carried out. Firstly, the relative intensity noises of three femtosecond laser sources were measured. Secondly, noise characterizations of the detection system were carried out and our findings prove that our SRS microscope is shot noise-limited, demonstrating that the third laser source introduction is well suited and satisfies our purpose. Finally, the statistical properties of the overall image noises are analyzed and discussed.

Keywords: nonlinear microscopy; SRS imaging; RIN; shot noise

Citation: Ranjan, R.; Costa, G.; Ferrara, M.A.; Sansone, M.; Sirleto, L. Noise Measurements and Noise Statistical Properties Investigations in a Stimulated Raman Scattering Microscope Based on Three Femtoseconds Laser Sources. *Photonics* **2022**, *9*, 910. https://doi.org/10.3390/photonics9120910

Received: 16 October 2022
Accepted: 24 November 2022
Published: 28 November 2022

1. Introduction

Stimulated Raman scattering is a dissipative process in which energy is transferred from input photons to molecular vibrations. From a quantum mechanical point of view, SRS can be described as a two-photon stimulated process, in which one pump photon at frequency ω_p is annihilated (stimulated Raman loss, SRL), and one Stokes photon at frequency ω_s is emitted (stimulated Raman gain, SRG). At the same time, the materials make a transition from the electronic ground state to a vibrationally excited state. Nowadays, SRS presents an important perspective in a number of fields, among them are nanophotonics [1–5], bio-photonics [5–10], and materials science [11].

One of the fascinating nanophotonics applications is the realization of integrated laser sources. In Raman lasers (RLs), coherent lights at any desired wavelength can be achieved by a proper choice of the pump wavelength, when the pump and Stokes wavelengths are within the transparency region of the gain material. For the future, the big challenge is the realisation of a nanoscale low-powered silicon (Si) Raman laser while maintaining a high level of performance [1–5].

Label-free SRS microscopy can perform *label-free* imaging with high spatial and spectral resolution, high sensitivity, 3D sectioning, and fast image acquisition time (a few seconds). In SRS microscopy, the images of a variety of molecular species, with chemical bonds in all the region of Raman spectra, i.e., C-H region (>2800 cm^{-1}), silent region (1800–2800 cm^{-1}), and fingerprint region (<1800 cm^{-1}), can be obtained [5–10]. However, many biomolecular species share similar chemical bonds in SRS microscopy, so the detection specificity can

be compromised. In recent times, in order to overcome this limitation, a bio-orthogonal chemical imaging platform has been explored, obtained by coupling SRS microscopy with small and Raman-active vibrational probes. They exhibit sensitivity, specificity, and biocompatibility for small-molecule imaging, but the most appealing advantage is that their Raman peaks belong to the silent region, where peaks coming from endogenous molecules are not present [12–15]. On the other hand, in [16], a significant improvement in the stimulated Raman signal obtained by femtosecond pulse excitation was achieved with respect to picosecond pulse. In the last few years, several biological applications have been reported [17–25] based on femtosecond stimulated Raman microscopy plus bio-orthogonal chemical imaging platforms. These achievements extend SRS microscopy to the silent region and provide a unique perspective for improving the specificity of SRS microscopy. SRS spectroscopy/microscopy is particularly attractive for investigating material structures, too. In the last few years, SRS spectroscopy has been applied to a number of systems in materials science, including 2D materials, interfacial structures, and dynamic chemical reactions [11].

However, since the Raman cross-section of the molecules is weak, SRS spectroscopy/microscopy can suffer from a low signal-to-noise ratio (SNR). Indeed, in the SRS technique, an alternative current (AC) signal at the sub-microvolt level has to be extracted from a noisy environment. We note that being the shot noise, a detected light intrinsic property, the best experimental condition is obtained when the shot noise is the dominant noise contribution. When the optical power is of the order of several milliwatts, the thermal noise is negligible compared to the shot noise, so in SRS, by using low-intensity laser noise and beam modulation frequencies at frequencies above 1 MHz, the shot noise regime can be obtained. Generally, for methods relying on detecting weak modulation of large signals, lock-in detection is used. Using a modulation technique and lock-in detection, sensitivity levels can be pushed to the shot noise limit and a small number of SRS active molecules' ensembles can be measured [26–33].

In order to explore the large variety of SRS applications, the two lasers should be able to cover all the regions of Raman spectra, i.e., both the wavelength windows of interest for nano- and bio-photonics application and, in addition, to deliver suitable laser power levels in order to achieve the highest signal to noise ratio. Although the two lasers usually have a large and independent tunability, it is still an issue to satisfy all the requirements listed above.

For femtosecond nonlinear spectroscopy/microscopy implementations, one of the most utilized laser combinations is given by a Ti:Sa plus IR-OPO (infrared radiation-optical parametric oscillator). Typically, its tunability allows covering visible and near-infrared spectra (until 1600 nm) and to investigate both the windows of wavelength of interest for biological and photonics applications. Still, in the case of SRS, its drawback is that only the C-H region (>2500 cm^{-1}) can be explored. This means that the demand, for example, for a biorthogonal platform cannot be accomplished [34–40].

Starting from this combination of laser sources, in our previous paper, a femtosecond stimulated Raman scattering spectroscopy/microscopy implementation, equipped with three femtosecond laser sources, was presented. Our system covered all the regions of Raman spectra, taking advantage of two possible laser combinations. The first combination, a titanium–sapphire (Ti:Sa) oscillator plus an optical parametric oscillator (OPO), covers in SRG modality the C-H region (>2800 cm^{-1}), while the second combination, a Ti:Sa oscillator plus a second harmonic generator (SHG), covers in SRL modality the C-H region and the fingerprint region. Evidently, the proposed implementation allows all of the requirements that we have mentioned before to be satisfied, i.e., exploring the window of wavelength of interest for photonics applications and all the biological Raman spectra regions, overcoming the limitation of combination Ti:Sa plus IR-OPO [41].

In this paper, to prove the reliability of our proposed SRS microscope, based on three femtoseconds laser sources, noise measurements were carried out. Firstly, single beam characterizations were reported. Since the intensity fluctuations of the laser can exceed

the shot noise and/or the thermal noise of the photodetector, the relative intensity noise (RIN) of each femtosecond laser source was measured. In addition, each femtosecond laser source was characterised by autocorrelation measurements. Secondly, since in an LIA the output signal can appear in the input signal noise near the reference frequency, the noise influencing the detection system was measured. Finally, statistical analysis of images noises was performed and a correlation along the fast axis of background noise was demonstrated.

2. Experimental Setup and Methods

In our previous paper [41], a femtosecond stimulated Raman scattering (*fs*-SRS) microscope equipped with three femtosecond laser sources was reported. The microscope was obtained by the integration of a femtosecond stimulated Raman spectroscopy set up with a C2 Nikon microscope, provided with a fast mirror scanning unit (Figure 1). The main characteristics of the lasers are listed below in Table 1.

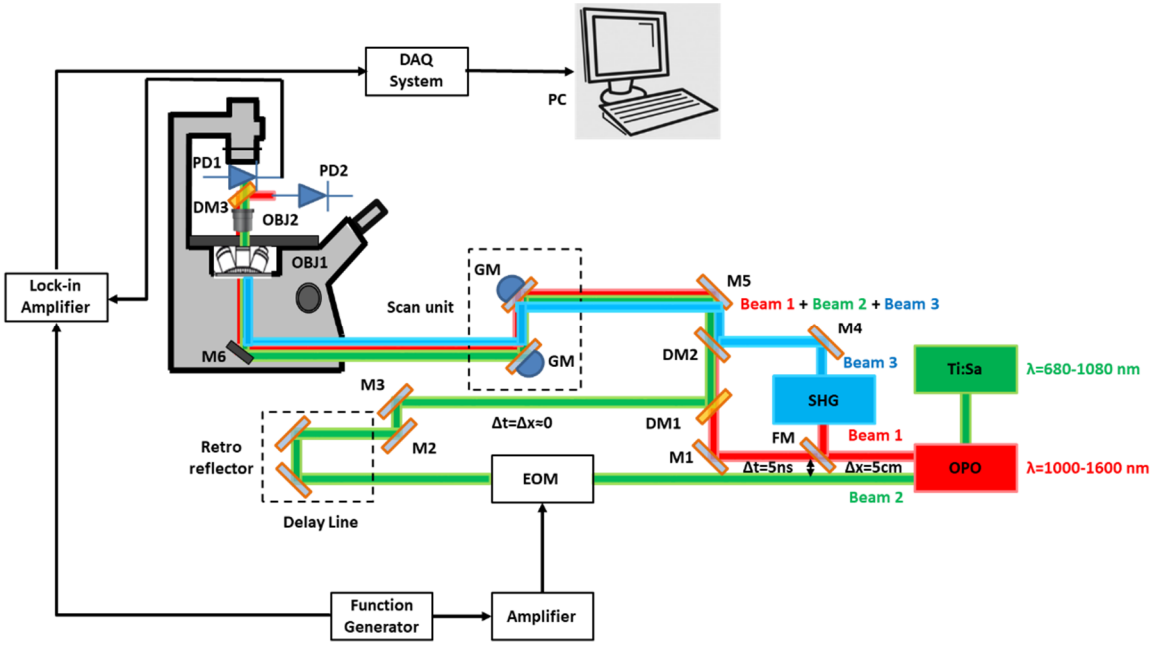

Figure 1. Experimental setup. Ti:Sa = titanium–sapphire (Ti:Sa) oscillator; OPO = optical parametric oscillator; SHG = second harmonic generation, M1-M6 = femtoseconds mirrors; FM = flip mirror; DM1, DM2, DM3 = dichroic mirrors; EOM = electro-optic modulator; GM = galvo mirrors; OBJ1, OBJ2 = objective lens; PD1 = photodiode (Si detector) for SRL measurements; PD2 (InGaAs detector) for SRG measurements.

Table 1. The lasers' properties.

Laser	Wavelength Range	Pulse Durations	Repetition Rate
Ti:Sa	740 nm–880 nm	140 fs	80 MHz
OPO	1000 nm–1600 nm	200 fs	80 MHz
SHG	500 nm–800 nm	200 fs	80 MHz

We note that in our implementation, the integration of stimulated Raman gains and stimulated Raman losses detection modes in a single nonlinear microscope was demonstrated for the first time. Our system had the merit to allow generating images of the same region in succession in SRL and SRG modalities without adding or removing components. A few years later, an SRS system able to simultaneously generate images of the same region in SRL and SRG modalities was presented in [42,43], although with different motivations and characteristics.

In order to characterize the femtosecond sources for each of them, laser noise and pulse duration measurements were performed. In Figure 2, the setup used for such measures is reported.

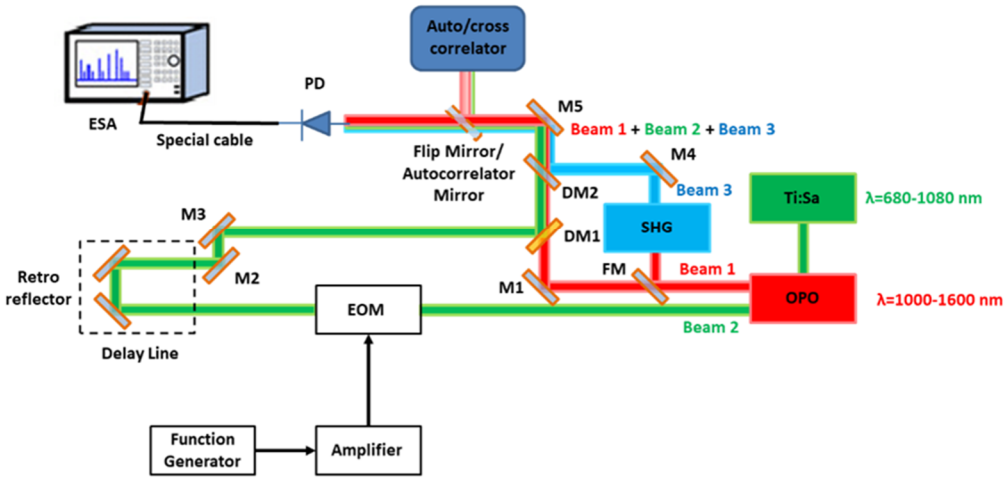

Figure 2. Experimental setup for femtosecond laser sources characterization. Ti:Sa = Ti:Sa laser; OPO = optical parametric oscillator; SHG = second harmonic generation; M1-M5 = femtosecond mirror; FM = flip mirror; DM1, DM2 = dichroic mirror; EOM = electro-optic modulator; PD = photodiode; ESA = electronics spectrum Analyzer.

The output pulses in any pulsed laser are not a perfect replica of each other but some unexpected changes in the pulse properties are usually exhibited. Intensity noise is the fluctuation in the average power of optical pulse trains over a certain measurement time span, representing the average power stability of the optical pulse train. The excess noise contribution for pulsed lasers depends on the modulation of laser frequency. In fact, while the thermal noise and the shot noise power do not rely on the laser modulation frequency, the excess noise has a $1/f$ behaviour. For modulation frequencies below the 100 kHz limit, the excess noise is dominant, while, as the modulation frequency increases, it becomes negligible with respect to the other two noise sources.

The intensity noise is quantified as the RIN describing the intensity fluctuations of the laser to the receiver's electrical noise relative to the signal power observed electrically [44]. It can be measured by detecting the laser beam by a fast photodetector and processing the detector output with a radiofrequency electronic spectrum analyzer (RF-ESA). In our setup, to measure the relative intensity noise of Ti:Sa, OPO, and SHG laser sources, a fast photodiode (PD) was inserted after the mirror, namely M5 (Figure 2). The PD is connected to an RF-ESA using a special cable avoiding external perturbations.

In our experiment, the duration of short pulses is estimated, performing autocorrelations measurements, based on two-photon absorption (TPA). In the TPA process, a photocurrent is generated proportional to the square of the input light intensity, when the photon energy ($h\nu$) of incident light satisfies the condition, $2\ h\nu > Eg$ (where Eg is the bandgap energy of the material). TPA is an efficient, fast, and broadband nonlinear process which does not require phase-matching [45]. In our optical setup, to measure the pulse duration of the beams, a flip-flop mirror after the mirror M5 is introduced (see Figure 2), which allows diversion of the laser beam toward an auto-correlator (pulseCheck 50-APE, Berlin, Germany).

We note that an LIA, with its high signal-to-noise ratio and sensitivity due to its phase-sensitive detection, is appropriate for SRS measurements. An LIA is a bandpass amplifier with an adjustable central frequency measuring the signal amplitude close to a given reference frequency (f) with a defined narrow frequency bandwidth around it. In an LIA, the filter's equivalent noise bandwidth (ENBW) for a time constant T and a slope of 18 dB/octave is given by the formula $3/(32T)$. In our LIA in the frequency range of

100 kHz–100 MHz (with 50 Ω input), the typical input noise has a maximum value of 4 nV/$\sqrt{}$Hz.

3. Results and Discussion

In order to perform noise measurements, typical operating conditions for biological applications of our SRS microscope have been used, particularly for Ti:Sa, OPO, and SHG wavelengths, power incident onto the detector, and the modulation frequency (5 MHz) of the pump in SRG modality and of the probe in SRL modality.

In our measurements, with the RIN being proportional to the power, the laser beam's power was fixed at 10 mW. As RIN is a function of frequency, to minimize the laser's RIN, the choice of the laser modulation frequency is fundamental. In Figure 3 the RIN measurements in the range of frequencies [1 MHz–10 MHz] of OPO at 1076 nm, Ti:Sa at 810 nm, and SHG at 650 nm, obtained by an RF-ESA, are reported.

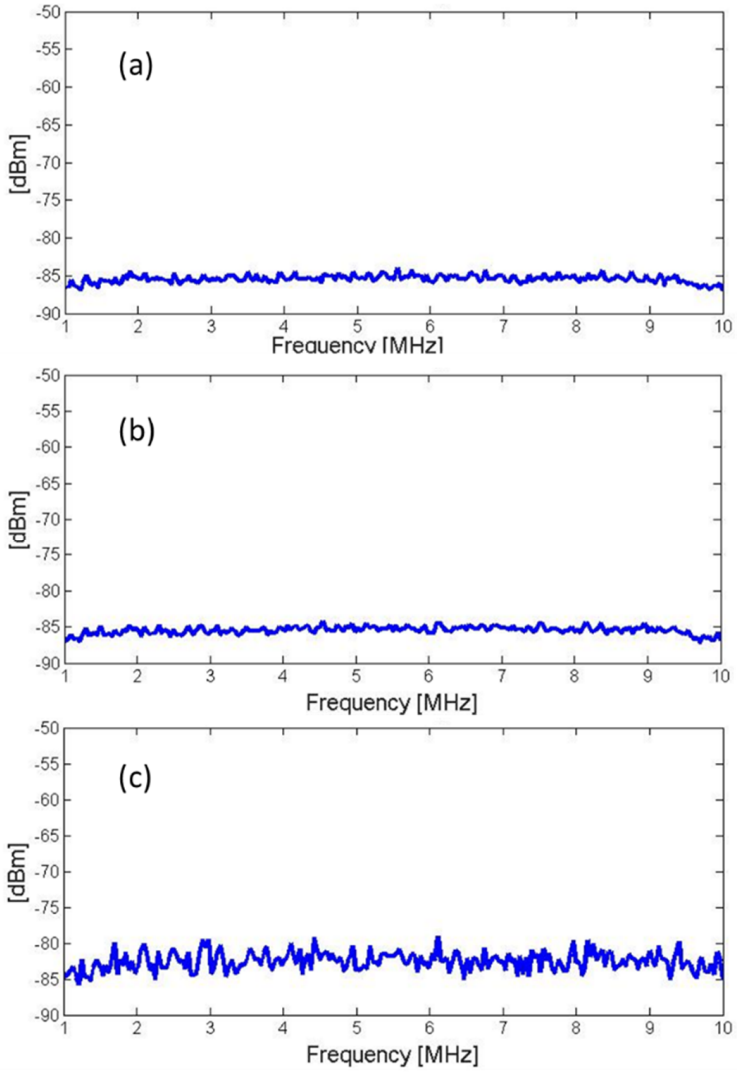

Figure 3. Relative intensity noise (RIN) measurements for three laser sources: (**a**) OPO; (**b**) Ti:Sa; (**c**) SHG.

However, it is clearly visible in Figure 3 that the RIN of all of the considered laser beams is flat in the range of 1–10 MHz. This means that the shot noise regime at the operating modulation frequency of our microscope, that is 5 MHz, is achieved for all three sources.

The collected autocorrelation functions of Ti:Sa, OPO, and SHG are reported in Figure 4a–c, respectively. As expected, the pulses show a Gaussian-like distribution and evaluate the pulse width value. All the autocorrelation traces were Gaussian-fitted. The corresponding full width at half-maximum (FWHM) of the Gaussian curves was calculated to be about 341 fs, 330 fs, and 357 fs for Ti:Sa, OPO, and SHG, respectively. The FWHM of the unknown pulse τ_p is proportional to the FWHM of the measured fringe-resolved intensity autocorrelation function τ_{ac}:

$$\tau_{ac} = k \cdot \tau_p \quad (1)$$

where k is the proportionality factor, also known as the deconvolution factor. k differs significantly for different pulse shapes and Gaussian shapes, $k = 1.414$ [46].

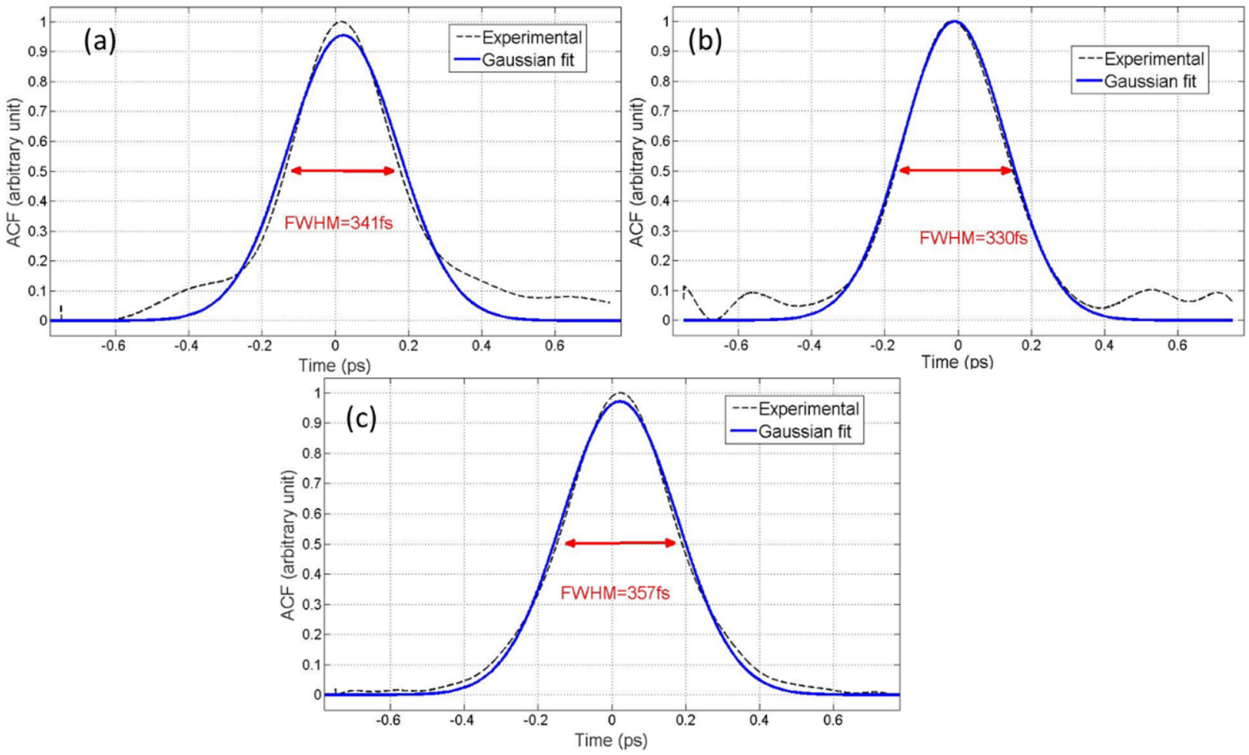

Figure 4. Autocorrelative characterization and corresponding Gaussian fit of the three sources: (**a**) Ti:Sa; (**b**) OPO; (**c**) SHG.

Considering Equation (1), the values of the pulses' width at the input of the microscope were about 241 fs for Ti:Sa, about 233 fs for OPO, and about 253 fs for SHG. Thus, with respect to the values reported in Table 1, a significant broadening for Ti:Sa was observed, which can be explained considering that a Pockels cell is employed in its optical path. On the contrary, a slight broadening was observed for OPO, and the same was observed for the change induced by SHG with respect to OPO.

The noise in the SRL detection mode of our SRS detection system was measured with SHG pulses impinging on the PD while Ti:Sa pulses were stopped. The wavelength of SHG was fixed at 650 nm, while its optical power was increased. For each power value, ten lock-in measurements were acquired. For each measurement, the sensitivity of LIA was fixed to 10 µV, the acquisition time was 16 s, and the LIA time constant was set to 100 µs with an 18 dB/oct slope. The standard deviation normalized to the lock-in gain and to the bandwidth is shown in Figure 5.

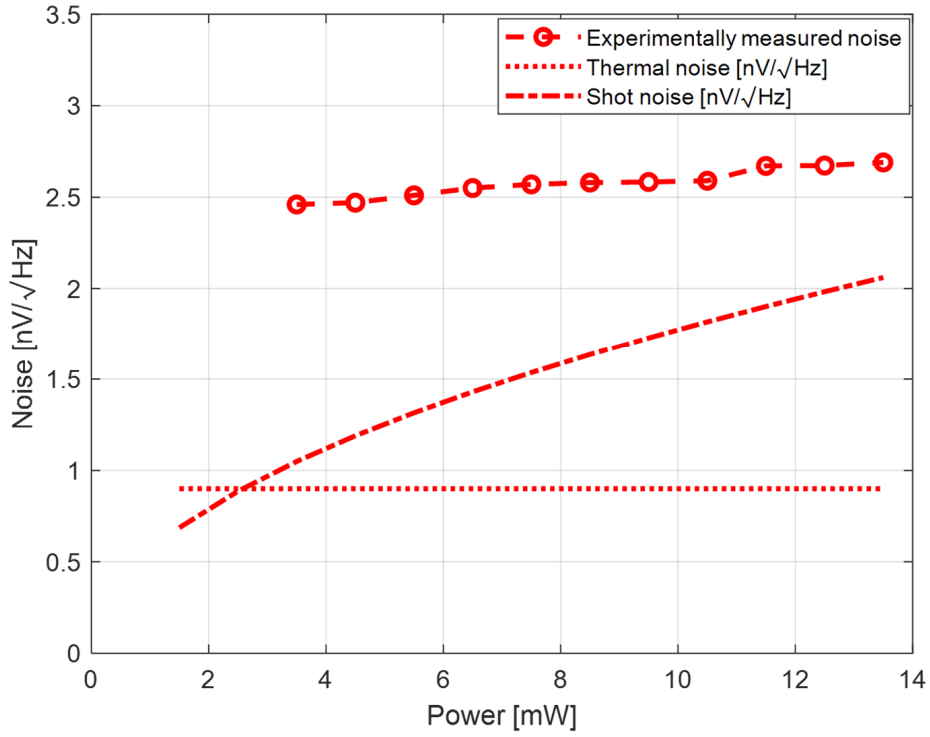

Figure 5. Calculated noise and experimentally measured noise as a function of laser power in the range from 1.5 to 13.5 mW with the steps of 1 mW.

In Figure 5, the thermal noise and the shot noise are reported. The Johnson noise is prevailing when the laser power is lower than 2.5 mW, but when the laser power is increased, the shot noise surpasses the thermal noise. Therefore, our system is shot noise-limited in the range from 2.5 to 13.5 mW. Taking into account that the typical value of input noise of a good low noise amplifier is about 3 $nV/\sqrt{Hz}$, we can conclude that our system is truly a state-of-the-art tool.

To investigate the statistical properties of image noise, two sets of 10 images with background noise, i.e., in off-resonance, in SRL modalities, with a fixed power impinging on the PD of 10 mW, were acquired. Each image was a single recording of 512 px × 512 px. For each image, the sensitivity of LIA was fixed to 10 µV, the time constant was set to 100 µs with an 18 dB/oct slope. The only difference between the two sets of images was the acquisition times: 8 s for the first set and 16 s for the second one.

In order to investigate the hypothesis of uncorrelation, for each set, on both the fast axis and slow axis of all of the images (j = 1, . . . 10), the Ljung-Box Q-test (LBQ test) [46,47] was applied. The confirmation percentage was fixed at 95% in order to accept the hypothesis of uncorrelation along the directions taken into account. For each set, the percentage of uncorrelation along the fast axis was 0.2% and the uncorrelation hypothesis was rejected. On the contrary the percentage of uncorrelation along the slow axis was ≈99% and the uncorrelation hypothesis was accepted.

Evidently, the noise correlation along the fast axis was revealed by the LBQ analysis. In the case of a noise image with an acquisition time of 8 s, in Figure 6, a strong correlation between consecutive pixels along the fast axis was reported, which dropped to zero after 6 pixels.

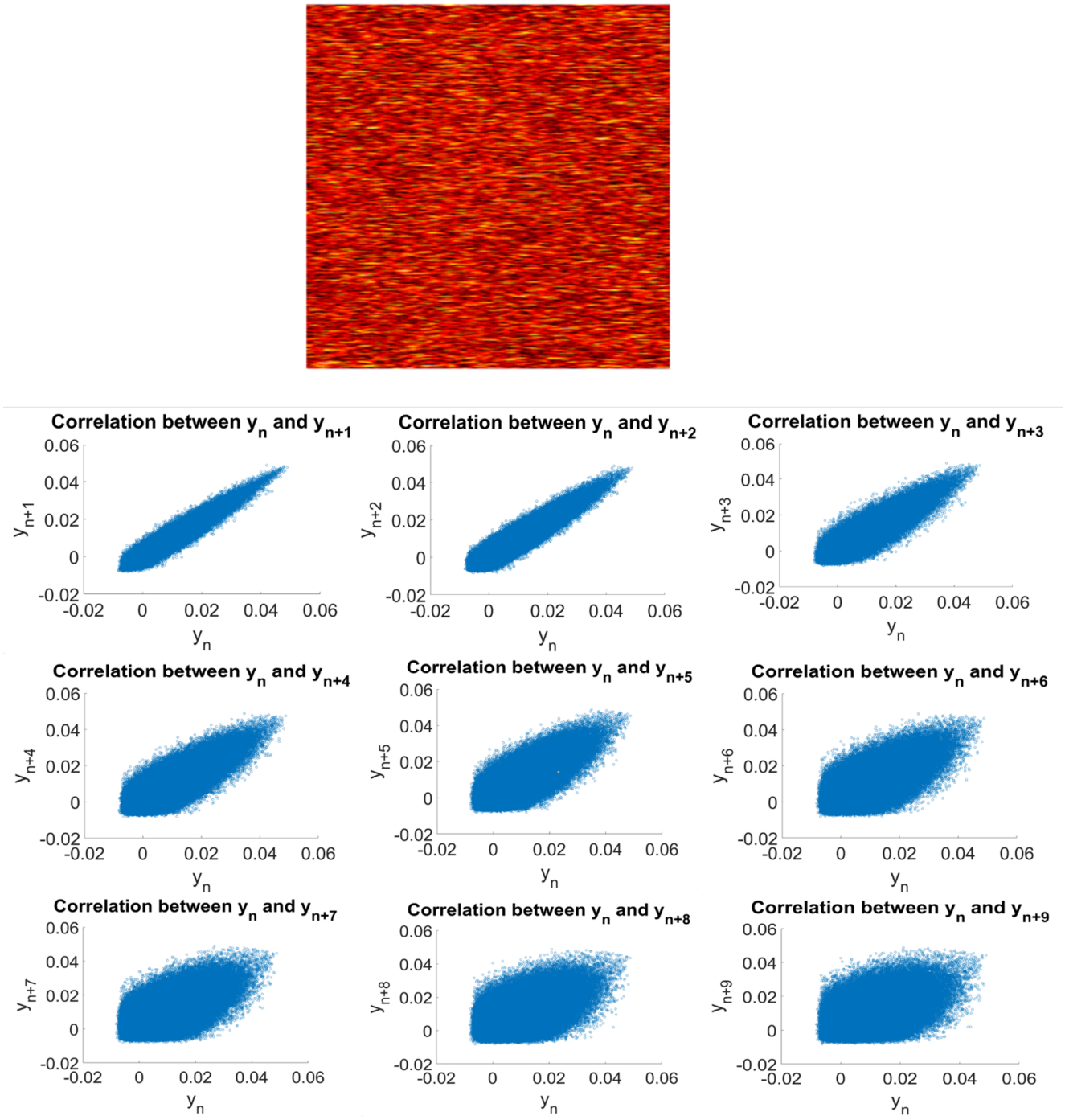

Figure 6. Scatter plots of two pixels along the fast axis. In each plot, *y_n* is the value of a pixel at column *n*. The image was acquired with an acquisition time of 8 s.

In the case of a noise image with an acquisition time of 16 s, in Figure 7, the noise correlation between adjacent pixels along the fast axis is reported. A strong correlation between three consecutive pixels is pointed out, dropping to zero after 3 pixels.

Finally, we consider a set of noise acquisitions obtained without lock-in and with no incident power on the PD, whose output signal is directly connected to the PCI card. In this case, no correlation was found regardless of the time of acquisition of noise images, in Figure 8.

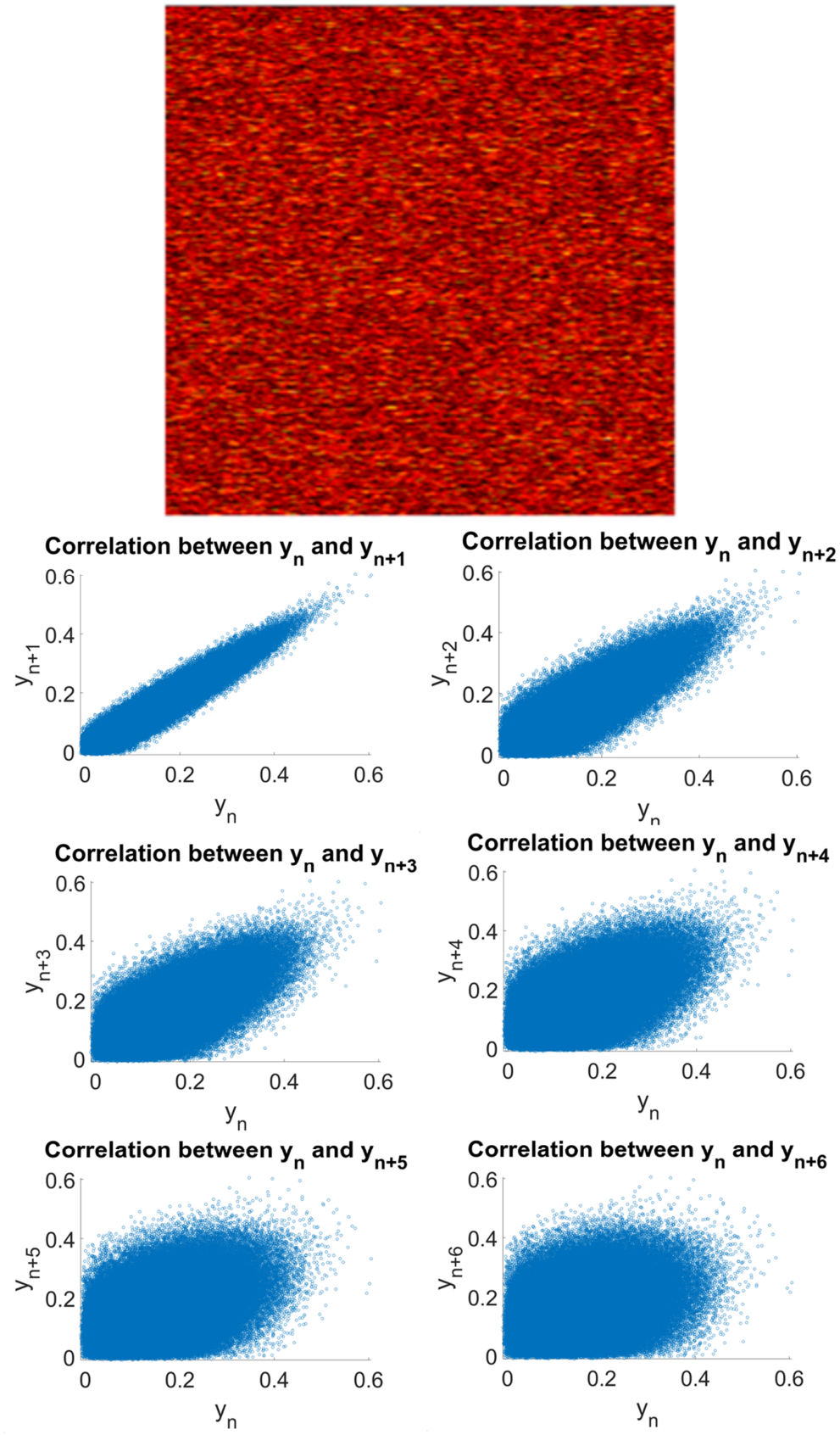

Figure 7. Scatter plots of two pixels along the fast axis. In each plot, y_n is the value of a pixel at column n. The image was acquired with an acquisition time of 16 s.

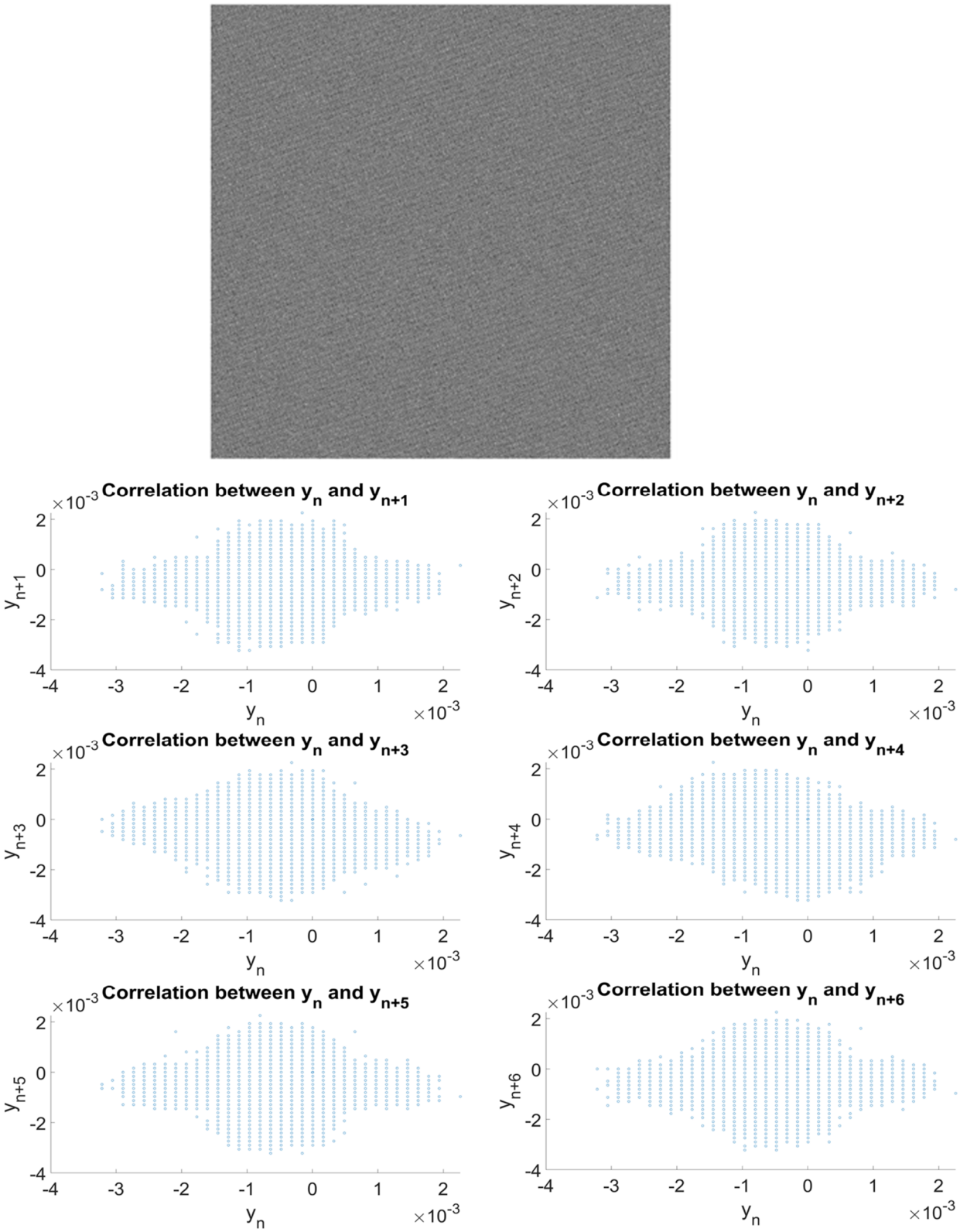

Figure 8. Scatter plots of two pixels along the fast axis. In each plot, *y_n* is the value of a pixel at column *n*. The image was acquired with an acquisition time of 16 s.

The correlation along the fast axis is due to the difference between the time constant of the lock-in amplifier and the pixel dwell time. Our results prove that the number of the consecutive correlated pixel can be approximately obtained by the ratio between the

LIA time constant (in our case, 100 µs) and the pixel dwell time, which was 30 µs for an acquisition time of 16 s and 15 µs for an acquisition time of 8 s. There are no correlations along the slow axis, since the time gap between two pixels along the column (given by 516 multiplied by pixel dwell time) is bigger than the lock-in amplifier time constant.

Our results from the statistical analysis confirm the general rule claiming that the lock-in bandwidth should match the pixel acquisition rate in order to distinguish fluctuations from one pixel to the next. However, it is worth noting that matching the conditions is not achievable for most of the SRS microscopes. Therefore, statistical analysis of background noise, which is generally overlooked in the literature, is a fundamental step toward optimizing SRS images' denoising.

4. Conclusions

Our results of laser intensity noise measurements demonstrate that Ti:Sa, OPO, and SHG beams are shot noise-limited in the range of interest {1–10} MHz. Autocorrelation measurements confirm that the beam obtained by SHG preserves the pulse duration of OPO. Finally, the shot noise-limited condition for our microscope has been proven, hence a standard single-channel silicon photodiode can be applied to detect SRS signals and no sophisticated detection techniques, such as balanced heterodyning, are required. Evidently, we demonstrate that the introduction of a third femtosecond laser source is well suited and satisfies our purpose, with the performances of our SRS microscope being preserved in both SRG and SRL modalities.

Our statistical analysis proves that correlated noise can affect the imaging system, even if a shot noise-limited condition is demonstrated by spectroscopy measurements. This is a crucial point that is usually overlooked. It is worth noting that, in SRS literature, the hypothesis of white noise, generally supposed by many denoising algorithms, is assumed after the shot noise-limited condition has been proven by spectroscopic measurements. We note that this point was raised for the first time in our previous paper [40]. However, here a more complete discussion is provided. In our previous paper, this correlation was demonstrated for SRG modality, while here it is demonstrated for SRL modality, too. The beams' wavelengths of detected noise were different (1076 in the previous paper and 650 in this one). In this paper, different times of image acquisition were considered, demonstrating the link between the time acquisition of the image and the pixel dwell time. Finally, the experimental result obtained considering an acquisition chain without lock-in was reported and discussed.

We note that a crucial point for SRS biological applications is the fidelity of SRS images, because it can be impaired by noise sources, limiting the achievable contrast and sensitivity, and by competitive effects, producing artifacts. The SRS signal is generated at the frequency of incident beams acting as local oscillators. Such heterodyne detection boosts the signal level and removes the non-resonant background encountered in CARS microscopy. For this reason, initially, it was suggested that SRS microscopy was free of spurious background signals. Of course, this is true only in a relative sense; the SRS signal is in general overlaid with parasitic signals stemming from various linear (scattering and absorption) and nonlinear optical effects whose sources are ubiquitous. Due to other nonlinear optical processes, unwanted signals can be classified into two major types: nonlinear transient absorption (TA) and nonlinear transient scattering processes. Both are heterodyne modalities, producing a spectrally overlapped background with the SRS signal. A possible option in order to remove these effects is to evaluate both the stimulated Raman loss and the stimulated Raman gain, as these two contributions should be equal in the absence of artifacts. Recently, an SRS measurement method termed "stimulated Raman gain and loss opposite detection" (SRGOLD) [43] was proposed to reduce the SRS artifacts and to obtain a twofold increase in the magnitude of the SRS signal. Previous considerations suggest that it is advantageous to have SRL and SRG images separately to evaluate and compare their respective artifact contributions. Detecting the energy transfer from the pump to the Stokes and from the Stokes to the pump allows us to exploit the

full signal strength inherent to the SRS process. In [42], an SRS scheme named SRGAL (stimulated Raman gain and loss) was proposed, allowing for a quantitative evaluation of the SRS artifacts.

Evidently, our system has two main merits. The former being that it allows exploration of, in principle, a number of applications in different fields of nanophotonics, biophotonics, and material science; the latter being that it allows implementation of flexible tools [42], which are able to take on the formidable challenge of obtaining high-quality bioimaging removing unwanted background associated with target molecule signals. Both of these aspects contribute to paving the way to making SRS microscopy implementations cost-effective and reliable, thus encouraging their wide use not only in scientific laboratories.

Author Contributions: R.R. and L.S., M.S. conceived the experiments; R.R. and G.C., executed the experiments, and L.S., M.A.F. and M.S. supervised the experiments. R.R., G.C. and M.A.F. carried out the data analysis and study. R.R., L.S., M.A.F. and G.C. wrote the manuscript, and all authors revised it. This project was carried out under the leadership of L.S. All authors have read and agreed to the published version of the manuscript.

Funding: This research received no external funding.

Institutional Review Board Statement: Not applicable.

Data Availability Statement: The datasets generated during and/or analyzed during the current study are available from the corresponding author on reasonable request.

Conflicts of Interest: The authors declare no conflict of interest.

References

1. Sirleto, L.; Ferrara, M.A.; Nikitin, T.; Novikov, S.; Khriachtchev, L. Giant Raman gain in silicon nanocrystals. *Nat. Commun.* **2012**, *3*, 1220. [CrossRef]
2. Sirleto, L.; Vergara, A.; Ferrara, M.A. Advances in stimulated Raman scattering in nanostructures. *Adv. Opt. Photon.* **2017**, *9*, 169–217. [CrossRef]
3. Sirleto, L.; Aronne, A.; Gioffrè, M.; Fanelli, E.; Righini, G.C.; Pernice, P.; Vergara, A. Compositional and thermal treatment effects on Raman gain and bandwidth in nanostructured silica-based glasses. *Opt. Mater.* **2013**, *36*, 408–413. [CrossRef]
4. Ferrara, M.A.; Sirleto, L. Integrated Raman Laser: A Review of the Last Two Decades. *Micromachines* **2020**, *11*, 330. [CrossRef]
5. Sirleto, L.; Ferrara, M.A. Fiber Amplifiers and Fiber Lasers Based on Stimulated Raman Scattering: A Review. *Micromachines* **2020**, *11*, 247. [CrossRef]
6. Cheng, J.-X.; Xie, X.S. Vibrational spectroscopic imaging of living systems: An emerging platform for biology and medicine. *Science* **2015**, *350*, aaa8870. [CrossRef]
7. Camp, C.H., Jr.; Cicerone, M.T. Chemically sensitive bioimaging with coherent Raman scattering. *Nat. Photon.* **2015**, *9*, 295–305. [CrossRef]
8. Zumbusch, A.; Langbein, W.; Borri, P. Nonlinear vibrational microscopy applied to lipid biology. *Prog. Lipid Res.* **2013**, *52*, 615–632. [CrossRef]
9. Zhang, D.; Wang, P.; Slipchenko, M.N.; Cheng, J.-X. Fast Vibrational Imaging of Single Cells and Tissues by Stimulated Raman Scattering Microscopy. *Acc. Chem. Res.* **2014**, *47*, 2282–2290. [CrossRef]
10. Alfonso-García, A.; Mittal, R.; Lee, E.S.; Potma, E.O. Biological imaging with coherent Raman scattering microscopy: A tutorial. *J. Biomed. Opt.* **2014**, *19*, 071407. [CrossRef]
11. Cheng, Q.; Miao, Y.; Wild, J.; Min, W.; Yang, Y. Emerging applications of stimulated Raman scattering microscopy in materials science. *Matter* **2021**, *4*, 1460–1483. [CrossRef]
12. Wei, L.; Hu, F.; Chen, Z.; Shen, Y.; Zhang, L.; Min, W. Live-Cell Bioorthogonal Chemical Imaging: Stimulated Raman Scattering Microscopy of Vibrational Probes. *Acc. Chem. Res.* **2016**, *49*, 1494–1502. [CrossRef]
13. Hu, F.; Lamprecht, M.R.; Wei, L.; Morrison, B.; Min, W. Bioorthogonal chemical imaging of metabolic activities in live mammalian hippocampal tissues with stimulated Raman scattering. *Sci. Rep.* **2016**, *6*, 39660. [CrossRef]
14. Wei, L.; Hu, F.; Shen, Y.; Chen, Z.; Yu, Y.; Lin, C.C.; Wang, M.C.; Min, W. Live-cell imaging of alkynetagged small biomolecules by stimulated Raman scattering. *Nat. Methods* **2014**, *11*, 410–412. [CrossRef]
15. Wei, L.; Shen, Y.; Xu, F.; Hu, F.; Harrington, J.K.; Targoff, K.L.; Min, W. Imaging complex protein metabolism in live organisms by stimulated Raman scattering microscopy with isotope labeling. *ACS Chem. Biol.* **2015**, *10*, 901–908. [CrossRef]
16. Zhang, M.; Slipchenko, N.; Cheng, J.X. Highly sensitive vibrational imaging by femtosecond pulse stimulated raman loss. *J. Phys. Chem. Lett.* **2011**, *2*, 1248–1253. [CrossRef]
17. Zhang, C.; Li, J.; Lan, L.; Cheng, J.X. Quantification of lipid metabolism in living cells through the dynamics of lipid Droplets measured by stimulated Raman Scattering Imaging. *Anal. Chem.* **2017**, *89*, 4502–4507. [CrossRef]

18. Dou, W.; Zhang, D.; Jung, Y.; Cheng, J.-X.; Umulis, D.M. Label-free imaging of lipid-droplet intracellular motion in early Drosophila embryos using femtosecond-stimulated Raman loss microscopy. *Biophys. J.* **2012**, *102*, 1666–1675. [CrossRef]
19. Zhang, C.; Huang, K.-C.; Rajwa, B.; Li, J.; Yang, S.; Lin, H.; Liao, C.-s.; Eakins, G.; Kuang, S.; Patsekin, V.; et al. Stimulated Raman scattering flow cytometry for label-free single-particle analysis. *Optica* **2017**, *4*, 103–109. [CrossRef]
20. Li, J.; Cheng, J.-X. Direct visualization of De novo Lipogenesis in single living cells. *Sci. Rep.* **2015**, *4*, 6807. [CrossRef]
21. Shi, L.; Zheng, C.; Shen, Y.; Chen, Z.; Silveira, E.S.; Zhang, L.; Wei, M.; Liu, C.; de Sena-Tomas, C.; Targoff, K.; et al. Optical imaging of metabolic dynamics in animals. *Nat. Commun.* **2018**, *9*, 2995. [CrossRef]
22. Hu, F.; Chen, Z.; Zhang, L.; Shen, Y.; Wei, L.; Min, W. Vibrational imaging of glucose uptake activity in live cells and tissues by stimulated Raman scattering. *Angew. Chem. Int. Ed.* **2015**, *54*, 9821–9825. [CrossRef]
23. Long, R.; Zhang, L.; Shi, L.; Shen, Y.; Hu, F.; Zeng, C.; Min, W. Two-color vibrational imaging of glucose metabolism using stimulated Raman scattering. *Chem. Commun.* **2018**, *54*, 152–155. [CrossRef]
24. Zhang, L.; Shi, L.; Shen, Y.; Miao, Y.; Wei, M.; Qian, N.; Liu, Y.; Min, W. Spectral tracing of deuterium for imaging glucose metabolism. *Nat. Biomed. Eng.* **2019**, *3*, 402–413. [CrossRef]
25. Shen, Y.; Zhao, Z.; Zhang, L.; Shi, L.; Shahriar, S.; Chan, R.B.; Di Paolo, G.; Min, W. Metabolic activity induces membrane phase separation in endoplasmic reticulum. *Proc. Natl. Acad. Sci. USA* **2017**, *114*, 13394–13399. [CrossRef]
26. Ozeki, Y.; Dake, F.; Kajiyama, S.; Fukui, K.; Itoh, K. Analysis and experimental assessment of the sensitivity of stimulated Raman scattering microscopy. *Opt. Express* **2009**, *17*, 3651–3658. [CrossRef]
27. Ozeki, Y.; Kitagawa, Y.; Sumimura, K.; Nishizawa, N.; Umemura, W.; Kajiyama, S.S.; Fukui, K.; Itoh, K. Stimulated Raman scattering microscope with shot noise limited sensitivity using subharmonically synchronized laser pulses. *Opt. Express* **2010**, *18*, 13708–13719. [CrossRef]
28. Audier, X.; Heuke, S.; Volz, P.; Rimke, I.; Rigneault, H. Noise in stimulated Raman scattering measurement: From basics to practice. *Apl Photonics* **2020**, *5*, 011101. [CrossRef]
29. Moester, M.J.B.; Ariese, F.; De Boer, J.F. Optimized signal-to-noise ratio with shot noise limited detection in Stimulated Raman Scattering microscopy. *J. Eur. Opt. Soc. Rapid Publ.* **2015**, *10*, 15022. [CrossRef]
30. Nose, K.; Ozeki, Y.; Kishi, T.; Sumimura, K.; Nishizawa, N.; Fukui, K.; Kanematsu, Y.; Itoh, K. Sensitivity enhancement of fiber-laser-based stimulated Raman scattering microscopy by collinear balanced detection technique. *Opt. Express* **2012**, *20*, 13958–13965. [CrossRef]
31. Zada, L.; Fokker, B.; Leslie, H.A.; Vethaak, A.D.; de Boer, J.F.; Ariese, F. Stimulated Raman scattering simulation for imaging optimization. *J. Eur. Opt. Soc. Rapid Publ.* **2021**, *17*, 10. [CrossRef]
32. Zhang, C.; Zhang, D.; Cheng, J.-X. Coherent Raman Scattering Microscopy in Biology and Medicine. *Annu. Rev. Biomed. Eng.* **2015**, *17*, 415–445. [CrossRef]
33. Crisafi, F.; Kumar, V.; Scopigno, T.; Marangoni, M.; Cerullo, G.; Polli, D. In-line balanced detection stimulated Raman scattering microscopy. *Sci. Rep.* **2017**, *7*, 10745. [CrossRef]
34. Ranjan, R.; Ferrara, M.A.; Filograna, A.; Valente, C.; Sirleto, L. Femtosecond Stimulated Raman Microscopy: Home-built realization and a case study of Biological imaging. *J. Instrum.* **2019**, *14*, P09008. [CrossRef]
35. Ranjan, R.; Indolfi, M.; Ferrara, M.A.; Sirleto, L. Implementation of a Nonlinear Microscope Based on Stimulated Raman Scattering. *J. Vis. Exp.* **2019**, *149*, e59614. [CrossRef]
36. Ferrara, M.A.; Filograna, A.; Ranjan, R.; Corda, D.; Valente, C.; Sirleto, L. Three-dimensional label-free imaging throughout adipocyte differentiation by stimulated Raman microscopy. *PLoS ONE* **2019**, *14*, e0216811. [CrossRef]
37. D'Arco, A.; Ferrara, M.A.; Indolfi, M.; Tufano, V.; Sirleto, L. Label-free imaging of small lipid droplets by femtosecond-stimulated Raman scattering microscopy. *J. Nonlinear Opt. Phys. Mater.* **2017**, *26*, 1750052. [CrossRef]
38. D'Arco, A.; Brancati, N.; Ferrara, M.A.; Indolfi, M.; Frucci, M.; Sirleto, L. Subcellular chemical and morphological analysis by stimulated Raman scattering microscopy and image analysis techniques. *Biomed. Opt. Express* **2016**, *7*, 1853–1864. [CrossRef]
39. Sirleto, L.; Ranjan, R.; Ferrara, M.A. Analysis of Pulses Bandwidth and Spectral Resolution in Femtosecond Stimulated Raman Scattering Microscopy. *Appl. Sci.* **2021**, *11*, 3903. [CrossRef]
40. Ranjan, R.; Costa, G.; Ferrara, M.A.; Sansone, M.; Sirleto, L. Noises investigations and image denoising in femtosecond stimulated Raman scattering microscopy. *J. Biophotonics* **2022**, *15*, e202100379. [CrossRef]
41. Ranjan, R.; D'Arco, A.; Ferrara, M.A.; Indolfi, M.; Larobina, M.; Sirleto, L. Integration of stimulated Raman gain and stimulated Raman losses detection modes in a single nonlinear microscope. *Opt. Express* **2018**, *26*, 26317–26326. [CrossRef]
42. Heuke, S.; Lombardini, A.; Büttner, E.; Rigneault, H. Simultaneous stimulated Raman gain and loss detection (SRGAL). *Opt. Express* **2020**, *28*, 29619–29630. [CrossRef]
43. Berto, P.; Andresen, E.R.; Rigneault, H. Background-free stimulated Raman spectroscopy and microscopy. *Phys. Rev. Lett.* **2014**, *112*, 053905. [CrossRef]
44. Svelto, O.; David, C. *Hanna, Principles of Lasers*; Springer: Berlin, Germany, 2010; eBook; ISBN 978-1-4419-1302-9.
45. Chen, J.; Xia, W.; Wang, M. Characteristic measurement for femtosecond laser pulses using a GaAs PIN photodiode as a two-photon photovoltaic receiver. *J. Appl. Phys.* **2017**, *121*, 223103. [CrossRef]
46. Diels, J.C.M.; Fontaine, J.J.; McMichael, I.C.; Simoni, F. Control and measurement of ultrashort pulse shapes (in amplitude and phase) with femtosecond accuracy. *Appl. Opt.* **1985**, *24*, 1270–1282. [CrossRef]
47. Ljung, G.M.; Box, G.E.P. On a measure of lack of fit in time series models. *Biometrika* **1978**, *65*, 297–303. [CrossRef]